Traveling-Wave Photodetector Theory

Kirk S. Giboney, *Member, IEEE*, Mark J. W. Rodwell, *Member, IEEE*, and John E. Bowers, *Fellow, IEEE*

***Abstract*—Photodetector efficiency decreases as bandwidth increases. Bandwidth-efficiency limitations of traveling-wave photodetectors (TWPD's) are substantially greater than those of lumped-element photodetectors because the velocity-mismatch bandwidth limitation is independent of device length. TWPD's can be long for high efficiency without significantly compromising bandwidth. The TWPD is modeled by a terminated section of transmission line with a position-dependent photocurrent source propagating on it at the optical group velocity. A wave model for the transmission line confirms the accuracy of an equivalent-circuit model for electrical wave propagation. The velocity-mismatch impulse and frequency response are determined by absorption coefficient and wave velocities rather than junction capacitance and load resistance. The velocity-mismatch bandwidth limitations can be written in a simple form which elucidates the factors affecting device response. A discretized periodic TWPD is described by the same equations as the fully distributed version. This more complicated device offers additional degrees of freedom in design and potentially improved performance.**

***Index Terms*— High-speed circuits/devices, photodiodes, photodetectors, optical waveguides, optoelectronic devices, slow-wave structures, traveling-wave devices, ultrafast optoelectronics.**

I. Introduction

THE bandwidth-efficiency product of a photodetector imposes a bound on the speed and sensitivity of the photoreceiver in which it is used. Bandwidth-efficiency products of conventional vertically illuminated photodetectors (VPD's) are limited to about 40 GHz (in GaAs) [1]. The bandwidth-efficiency product can be improved by guiding the light perpendicular to the collection field, as in a waveguide photodetector (WGPD) or a traveling-wave photodetector (TWPD), so that absorption and carrier drift are orthogonal.

The TWPD is based on the WGPD, an in-plane illuminated photodetector in which transparent dielectric cladding layers about the absorbing core form a dielectric optical waveguide [1]–[6]. However, the TWPD is a distributed structure that overcomes the *RC* bandwidth limitation of the lumped-element WGPD. This is accomplished by implementing an electrode arrangement designed to support traveling electrical waves with characteristic impedance matched to that of the external circuit [7].

Manuscript received June 18, 1996; revised April 28, 1997. This work was supported by the DARPA Optoelectronics Technology Center and Ultra Program, and Rome Laboratories.

K. S. Giboney was with the Department of Electrical and Computer Engineering, University of California at Santa Barbara, CA 93106 USA. He is now with Hewlett-Packard Laboratories, Palo Alto, CA 94304 USA.

M. J. W. Rodwell and J. E. Bowers are with the Department of Electrical and Computer Engineering, University of California at Santa Barbara, CA 93106 USA.

Publisher Item Identifier S 0018-9480(97)05999-1.

TWPD bandwidth is limited by the optical absorption coefficient and the velocity mismatches between the optical wave and the forward- and reverse-traveling electrical (photocurrent) waves rather than an *RC* bandwidth limitation determined by the total junction area. For devices significantly longer than the absorption length, this bandwidth limitation is roughly independent of device length. This is why TWPD's can have larger bandwidth-efficiency products than are possible in lumped-element photodetectors.

The concept of the TWPD was first proposed in 1990 as a means to overcome the bandwidth-efficiency limits of conventional photodetectors [8]. Both p-n and Schottky junctions were briefly mentioned, although the several designs listed in the proposal were of the metal–semiconductor type. No detailed theory or experimental results from these designs have been reported.

In 1991, a velocity-matched p-i-n TWPD was proposed [9], although a quantitative theory of the effects of velocity matching on device response was not included in this report. Electrical waves generally propagate in a slow-wave mode on a p-i-n waveguide. Experiments derived from this proposal and directed toward high-power applications have recently been reported together with a frequency-domain analysis based on an equivalent-circuit model [10].

The theory of TWPD's, based on an equivalent-circuit model and quantifying the velocity-mismatch impulse response and associated bandwidth limitations was initially detailed in 1992 [7], and the first experimental demonstration of TWPD's followed in 1994 [11]. The TWPD's had significantly higher bandwidth-efficiency products than comparable WGPD's and VPD's on the same wafer, breaking records by large margins [12], [13]. The velocity-mismatch bandwidth limitation has been cast in a simpler form which affords physical insight and allows the use of standard design methods for TWPD's [7], [14].

TWPD's can be fabricated in many different configurations. The photodetector element can be a semiconductor p-i-n, Schottky, or metal–semiconductor–metal (MSM) diode. It can have gain, as in a photoconductor or avalanche photodetector. The geometry can be of any form in which the photodetector function is incorporated over the length of a simultaneous optical and electrical waveguide. The photodetector could be continuous over the length of the waveguides, as in a fully distributed TWPD. Alternatively, a passive or active optical waveguide periodically loaded by discrete photodetector elements is called a periodic TWPD. All TWPD's share the fundamental velocity-mismatch bandwidth limitation.

In this paper, a wave model for a fully distributed, parallel-plate, p-i-n TWPD provides the basis for the theory of dis-

tributed photodetection. Quasi-TEM propagation is verified and correspondence with an equivalent-circuit model is established. The velocity-mismatch impulse response is used to find the velocity-mismatch frequency response, and a simple approximation for the velocity-mismatch bandwidth limitation is derived. The resulting expressions are general and applicable to any TWPD. Theoretical performance of the periodic TWPD is then analyzed, considering advantages and disadvantages relative to the fully distributed TWPD.

II. Theory of Distributed Photodetection

A. Wave Model

A TWPD is generally much shorter than the electrical wavelengths that it is designed for, but much longer than its optical absorption length. The interaction of the optical and electrical waves, or photodetection, occurs over the relatively short optical absorption length. This length, together with the electrical and optical wave velocities, determines the device response. Thus a distributed, rather than lumped, model is required.

The fully distributed parallel-plate p-i-n TWPD allows an analytical representation and serves as a model for the electrical propagation characteristics [7]. This model is easily adapted to TWPD's using other types of photodetector elements, such as Schottky or MSM diodes. In addition to forming a photodiode, the metal-clad, p-i-n structure is a parallel-plate electrical waveguide, and double-heterostructure semiconductor layers form a planar dielectric optical waveguide. The parallel-plate configuration allows two-dimensional (2-D) analysis [15]–[17]. Coplanar and hybrid structures nominally require three-dimensional (3-D) analyses [18]–[26]; however, certain symmetries often permit an effective dimensional reduction [27]–[31].

The p-i-n TWPD structure is similar to metal–insulator–semiconductor (MIS) structures that have been extensively analyzed [15]–[31], and the general characteristics of the waves supported on these structures are similar. This is seen by assuming that the p and n layers of the TWPD are of equal conductivity and thickness, and then applying image theory. The waveguide is cut in half, as shown in Fig. 1(a), with an electric wall at the plane of symmetry. The p-i-n TWPD now looks like an MIS structure with a perfect conductor as the top metal. A thin (10-nm) contact layer is included in the model of Fig. 1 to simulate the metal–semiconductor junction.

This structure is analyzed by starting with the time-harmonic form of Maxwell's equations in linear media, using cosine-based phasors

$$\nabla \times \mathbf{E} = -j\omega\mu\mathbf{H} \tag{1a}$$

$$\nabla \times \mathbf{H} = j\omega\varepsilon\mathbf{E}. \tag{1b}$$

Low-loss dielectrics are assumed and conductivity is incorporated into the dielectric constant $\varepsilon = \varepsilon' - j\sigma/\omega$. The wave equation follows directly from (1)

$$\nabla^2\mathbf{H} + \omega^2\mu\varepsilon\mathbf{H} = 0. \tag{2}$$

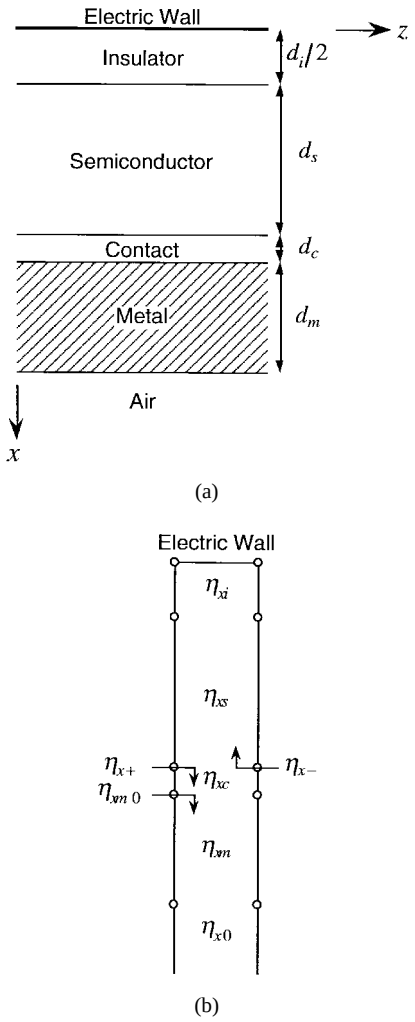

Fig. 1. TWPD half-waveguide (a) layer structure and (b) transmission-line equivalent circuit for transverse resonance. Waves propagate in the z-direction and are resonant parallel to the x-axis.

Electromagnetic waves will propagate only in the transverse-magnetic (TM) mode up to frequencies far above 1 THz in micron-dimension waveguides. Assuming no variation in the y-direction, the H-field is purely y-directed. The H-field for the nth layer is then

$$\mathbf{H}_n = \hat{y}\Big[H_{++n}e^{-j(k_{xn}x+k_zz)} + H_{+-n}e^{-j(k_{xn}x-k_zz)} + H_{-+n}e^{j(k_{xn}x-k_zz)} + H_{--n}e^{j(k_{xn}x+k_zz)}\Big] \tag{3}$$

where H represents the wave component amplitude, k_{xn} is the transverse propagation constant in the nth layer, and k_z is the longitudinal propagation constant. $k_n^2 \equiv \omega^2\mu_n\varepsilon_n = k_{xn}^2 + k_z^2$ is the dispersion relation. The transverse wave impedance of the nth layer is $\eta_{xn} = k_{xn}/\omega\varepsilon_n$. The electric fields are found directly from (1b).

A set of waves in the form of (3) satisfying the boundary conditions of the structure will propagate longitudinally (in the z-direction) and resonate transversely (in the x-direction). The transverse resonance condition is used to find the longitudinal propagation constant k_z, which characterizes the mode. Methods from mathematically equivalent, and perhaps

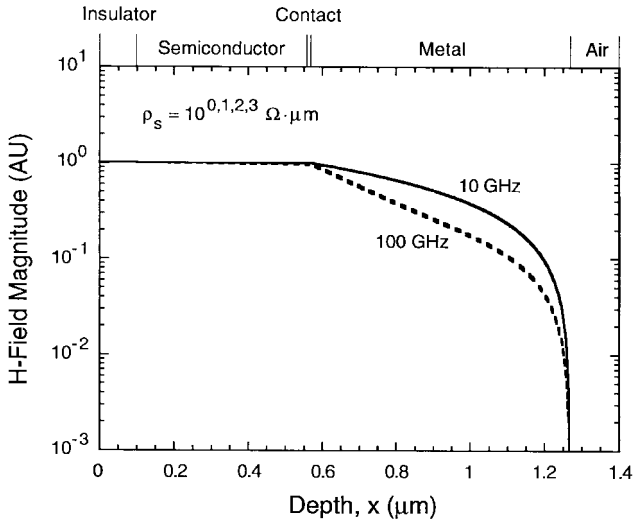

Fig. 2. Magnetic-field distribution in a parallel-plate TWPD at 10 and 100 GHz for a range of semiconductor layer resistivities of 1–1000 $\Omega\cdot\mu$m. The traces are coincident for all of the plotted semiconductor layer resistivities.

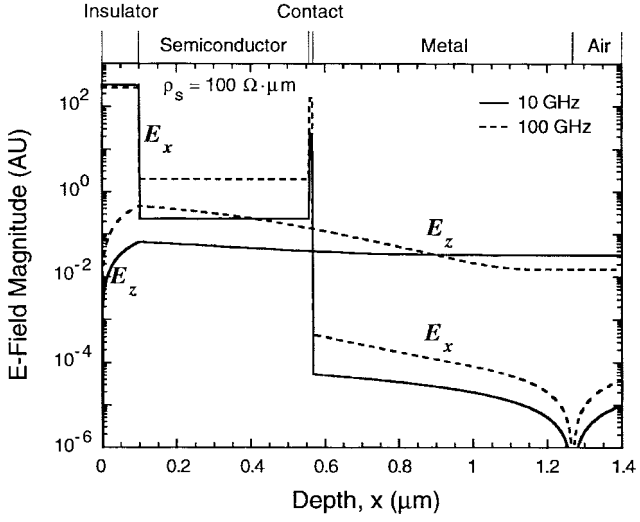

Fig. 3. Electric-field components in a parallel-plate TWPD at 10 and 100 GHz for semiconductor layer resistivity of 100 $\Omega\cdot\mu$m.

more familiar, transmission-line theory apply, and the problem can be analyzed using the transmission-line circuit analog for transverse resonance shown in Fig. 1(b).

The net impedance of the metal–air layers is reduced to a simple expression by assuming the wave impedance in the metal is much less than the transverse wave impedance in air, $\eta_m = \sqrt{j\omega\mu_0/\sigma_m} \ll \eta_{x0}$ [15]. The transverse wave impedance of the metal–air layers is then given by

$$\eta_{xm0} \approx \eta_m \coth\left[(1+j)\frac{d_m}{\delta_{sm}}\right] \tag{4}$$

where $\delta_{sm} = \sqrt{2/\omega\mu_0\sigma_m}$ is the skin depth in the metal. $\eta_{xm0} \to 1/\sigma_m d_m$ at low frequencies, and $\eta_{xm0} \to \eta_m$ at high frequencies.

The transverse resonance condition, $\eta_{x+} + \eta_{x-} = 0$, is

$$\eta_{xc}\frac{\eta_{xm0} + j\eta_{xc}\tan(k_{xc}d_c)}{\eta_{xc} + j\eta_{xm0}\tan(k_{xc}d_c)} + j\eta_{xs}\frac{\eta_{xi}\tan(k_{xi}d_i/2) + \eta_{xs}\tan(k_{xs}d_s)}{\eta_{xs} - \eta_{xi}\tan(k_{xi}d_i/2)\tan(k_{xs}d_s)} = 0. \tag{5}$$

This equation is solved numerically for k_z via the dispersion relation [32]. The electrical phase velocity and field attenuation constant are found from the real and imaginary parts of k_z. The insulator and semiconductor layer thicknesses are chosen such that a 1-μm-wide waveguide will have a characteristic impedance of about 50 Ω.

Field distributions in the waveguide are plotted in Figs. 2–4 for an insulator layer thickness of 0.2 μm. (The bandwidth limitation arising from the drift time of photogenerated carriers in a GaAs layer of this thickness is greater than 100 GHz.) The H-field magnitude at 10 and 100 GHz is plotted in Fig. 2. This plot shows that most of the current is carried in the metal layers, although the penetration into the metal decreases with increasing frequency. The current in the semiconductor layers increases slightly with frequency. Varying the resistivity of the semiconductor layers over three orders of magnitude produces little effect on the overall current distribution in the device.

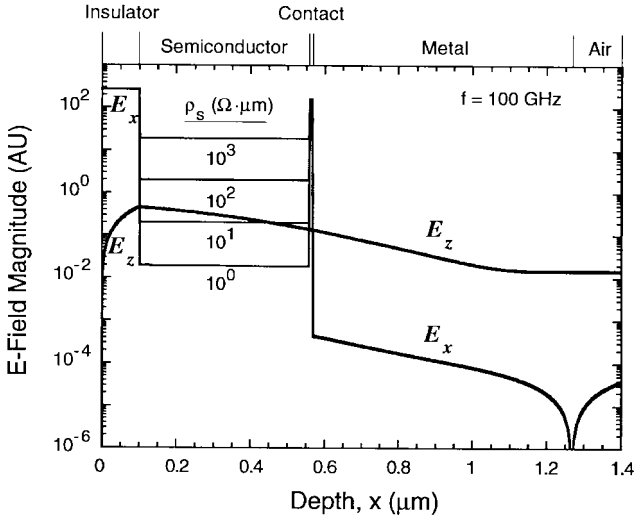

Fig. 4. Electric-field components in a parallel-plate TWPD at 100 GHz for semiconductor layer resistivities of 1–1000 $\Omega\cdot\mu$m.

The magnitudes of both E-field components at 10 and 100 GHz are plotted in Fig. 3 for a semiconductor resistivity of 100 $\Omega\cdot\mu$m, which is a typical resistivity for heavily doped semiconductor. Most of the voltage is supported by the insulator layer. Transverse fields in the semiconductor and metal layers and longitudinal fields in the insulator and semiconductor layers increase with increasing frequency. The change in longitudinal fields in the metal layers reflects the changing current distribution inferred from Fig. 2.

Fig. 4 shows the E-field components at 100 GHz for various semiconductor resistivities. The x-component in the semiconductor approaches the value in the metal as the resistivity is decreased, as expected. The z-component does not change significantly with semiconductor resistivity. Fields in the semiconductor and metal layers produce longitudinal and transverse currents, causing attenuation on the waveguide. Note that the x- and z-components are nearly equal in the semiconductor layers when the semiconductor resistivity is

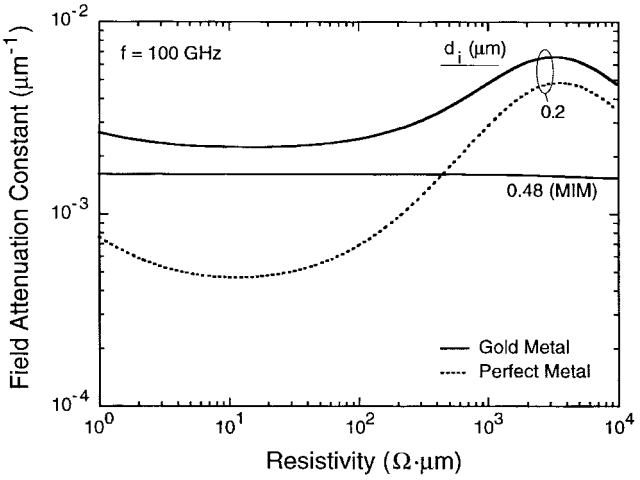

Fig. 5. Field attenuation constant as a function of semiconductor layer resistivity at 100 GHz. Curves for gold and perfect conductor metal layers cladding the parallel-plate p-i-n waveguide with insulator layer thicknesses of 0.2 μm are plotted. Attenuation of a gold MIM waveguide with insulator layer thickness of 0.48 μm (giving characteristic impedance of 50 Ω for a 1-μm-wide waveguide) is shown for comparison.

about 10 $\Omega\cdot\mu$m. This is approximately a point of minimum attenuation, evident in the plot of field attenuation constant versus semiconductor resistivity in Fig. 5. Also shown for comparison in Fig. 5 are plots of the attenuation constant of a waveguide with perfect metal rather than gold, and of a gold metal–insulator–metal (MIM) waveguide.

B. Equivalent-Circuit Model

The fact that E_x is much larger than E_z in the insulator, across which most of the voltage appears, together with the fact that the mode is TM, establishes that propagation on the TWPD is approximately TEM, or quasi-TEM. A transmission-line equivalent-circuit model accurately describes the properties of a quasi-TEM waveguide.

Such a circuit for a TWPD is shown in Fig. 6, and the element values for a parallel-plate TWPD are listed in Table I. Fig. 6(a) shows the physical origins of the circuit elements. Conduction and displacement currents in the contact and semiconductor layers are accounted for by resistances in parallel with capacitances, as shown in Fig. 6(b). At frequencies far below the dielectric relaxation frequencies of the contact and semiconductor layers ($\omega\rho_c\varepsilon_c \ll 1$ and $\omega\rho_s\varepsilon_s \ll 1$), the i-layer capacitance dominates the overall transmission line capacitance. While the i-layer capacitance is inversely proportional to the i-layer thickness, d_i, the inductance per unit length is proportional to the overall thickness between metal layers, $D\ (= d_i + 2(d_s + d_c))$. These dependencies on different thicknesses reflect the spatial separation of voltage and current which results in a slow-phase velocity and low characteristic impedance.

The z-component of the E-field in the metal layers is much larger than the x-component from Figs. 3 and 4, so waves in the metal propagate nearly parallel to the x-axis. Thus, the transverse wave impedance of the metal–air layers expressed in (4) is also the metal impedance listed in Table I for the equivalent circuit. The parallel conductance of the

TABLE I
PARALLEL-PLATE TWPD ELEMENT VALUES FOR THE EQUIVALENT-CIRCUIT MODEL IN FIG. 6

$Z_c = \dfrac{\rho_c}{1 + j\omega\rho_c\varepsilon_c}\cdot\dfrac{2d_c}{w}$	$Z_m = \eta_{xm0}\dfrac{2}{w}$
$Z_s = \dfrac{\rho_s}{1 + j\omega\rho_s\varepsilon_s}\cdot\dfrac{2d_s}{w}$	$G_s = \dfrac{\sigma_s}{3}\cdot\dfrac{wd_s}{2}$
$C_i = \varepsilon_i\dfrac{w}{d_i}$	$L_m = \mu_0\dfrac{D}{w}$

ρ is resistivity and $\sigma = 1/\rho$ is conductivity; ε and μ are permittivity and permeability. The metal–air transverse wave impedance η_{xm0} is defined in Fig. 1(b) and expressed in (4). w is the device width and $D = d_i + 2(d_s + d_c)$. Other dimensions are indicated in Fig. 1(a).

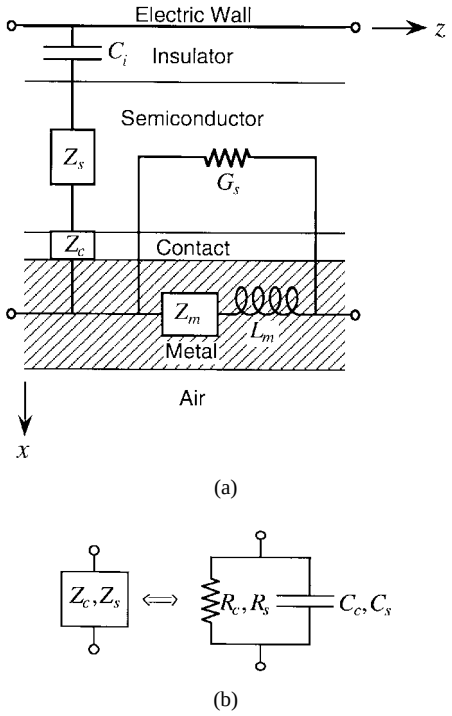

Fig. 6. TWPD equivalent-circuit models for (a) transmission-line characteristics and (b) semiconductor and contact layer impedances. Circuit elements are identified with their associated layers from Fig. 1. Element values for a parallel-plate TWPD are listed in Table I.

semiconductor layers G_s includes a divisor of three to account for the current distribution in the semiconductor layers [17].

The electrical wave velocity, field attenuation constant, and characteristic impedance calculated from the equivalent-circuit model are compared with those from the transverse resonance solution in Figs. 7–9 for semiconductor resistivities of 10, 100, and 1000 $\Omega\cdot\mu$m. The accuracy of the propagation constant from the equivalent-circuit model is excellent to beyond 1 THz because complex impedances were used to model the contact and semiconductor layers. The equivalent-circuit model also predicts characteristic impedance very well, aside from some deviation at high frequencies in the $\rho_s = 1000\ \Omega\cdot\mu$m traces. The accuracies shown in these plots hold with variations in

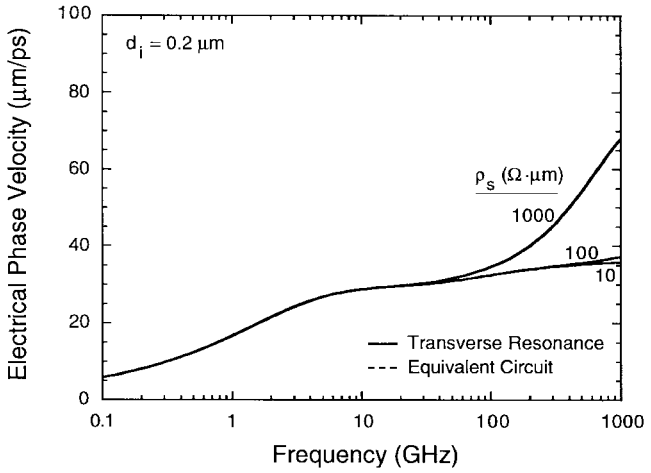

Fig. 7. Parallel-plate TWPD electrical velocity versus frequency from transverse resonance solution and equivalent circuit model for semiconductor layer resistivities of 10, 100, and 1000 $\Omega\cdot\mu$m. The full thickness of the insulator layer is 0.2 μm.

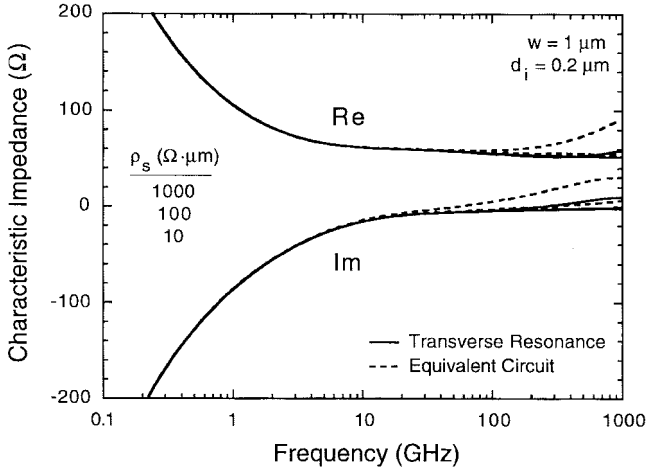

Fig. 9. Characteristic impedance of a 1-μm-wide parallel-plate TWPD from transverse resonance solution and equivalent circuit model. The traces are coincident over the range of plotted semiconductor layer resistivities except at high frequencies for both real and imaginary parts.

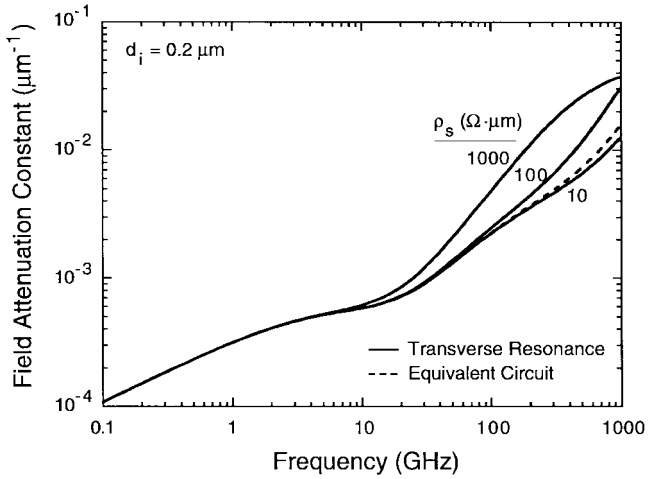

Fig. 8. Parallel-plate TWPD field attenuation constant, comparing transverse resonance solution and equivalent circuit model.

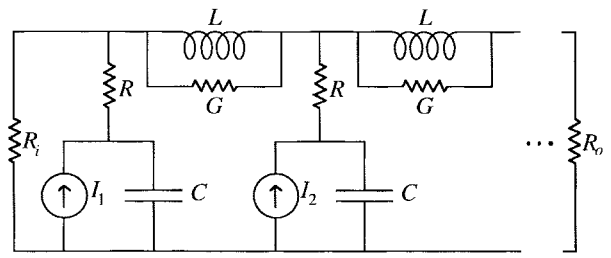

Fig. 10. TWPD equivalent circuit for midrange frequencies.

the insulator layer thickness as well, so the equivalent-circuit model can be considered generally reliable to 1 THz for the structures of interest here.

At frequencies far below the dielectric relaxation frequencies of the contact and semiconductor layers, the impedances of those layers are real and it is convenient to represent them as a resistor $R = R_c + R_s$. Also, the metal impedance does not significantly affect the propagation characteristics when $\omega L_m/Z_m \gg 1$. Thus, in the frequency range of critical interest, the TWPD is conveniently represented by the equivalent circuit of [7], reproduced here in Fig. 10.

The propagation characteristics in the mid-frequency range ($\omega L_m/Z_m \gg 1$, $\omega RC \ll 1$, and $\omega GL \ll 1$, covering from about 10 GHz to several hundred gigahertz in Figs. 7–9) are of greatest interest for TWPD's, since the device bandwidth falls within this range. The complex propagation constant can be written

$$\gamma_{\text{prop}} \approx \frac{\omega^2}{2v_e}(RC+GL) + j\frac{\omega}{v_e} \tag{6}$$

where $v_e \equiv \omega/\beta = 1/\sqrt{LC}$. The loss is proportional to the square of frequency, and consists of terms proportional to RC and GL. The minimum in Fig. 5 occurs when $RC = GL$. The characteristic impedance is

$$Z_0 \approx R_0\left[1 + j\frac{\omega}{2}(RC-GL)\right] \tag{7}$$

where $R_0 \equiv \sqrt{L/C}$. The effect of RC and GL on the characteristic impedance is to add a small reactance, which disappears when $RC = GL$. It is clear from (6) and (7) that the standard lossless transmission-line equations for phase velocity and characteristic impedance, $v_e = 1/\sqrt{LC}$, and $Z_0 = \sqrt{L/C}$ are good approximations for TWPD's.

C. Velocity-Mismatch Impulse Response

The TWPD velocity-mismatch impulse response is determined by the optical absorption coefficient and the mismatch between the optical group velocity and the forward- and reverse-photocurrent wave phase velocities [7]. The impulse response resulting from these effects, and no others, is derived here.

The TWPD is modeled by a terminated section of transmission line with an exponentially decaying photocurrent source propagating on it at the optical group velocity. Light absorbed in the i-layer generates electrical waves as an optical impulse propagates on the structure. Electrical waves propagate in both directions on the waveguide as they are produced by the

traveling photocurrent impulse source. The total forward-going electrical wave is composed of the wave which originally was forward-traveling, plus the wave which started out reverse traveling and was reflected at the device input end.

It is helpful to start in the inertial frame of reference of the forward-going electrical wave. The total forward-going charge density wave in the forward-going electrical wave frame of reference is

$$\rho(z',t) = \frac{Q}{2}\left[\Gamma\alpha' e^{-\Gamma\alpha' z'}u(z') + \gamma\Gamma\alpha'' e^{\Gamma\alpha'' z'}u(-z')\right] \quad (8)$$

where $Q = N_{\rm ph}\eta_i q$ is the total charge available in the optical impulse ($N_{\rm ph}$ is the number of photons in the impulse and η_i is the fraction of absorbed photons generating e–h pairs which are collected), Γ is the optical waveguide confinement factor, α is the i-layer material optical power-absorption coefficient, γ is the electrical reflection coefficient at the device input end, and u is the unit step function. Converting back to the device rest frame according to $z' = z - v_e t$, $\alpha' = \alpha/(1 - v_e/v_o)$, and $\alpha'' = \alpha/(1 + v_e/v_o)$ gives the forward-traveling charge density wave

$$\rho(z,t) = \frac{Q}{2}\left[\frac{\Gamma\alpha}{1 - v_e/v_o} e^{-\frac{\Gamma\alpha}{1-v_e/v_o}(z - v_e t)}u(z - v_e t) + \gamma\frac{\Gamma\alpha}{1 + v_e/v_o} e^{\frac{\Gamma\alpha}{1+v_e/v_o}(z - v_e t)}u(v_e t - z)\right]. \quad (9)$$

The current at the device output is the total forward-going charge density wave profile times the electrical wave velocity, $i(t + \ell/v_e) = \rho(z, t + z/v_e)\cdot v_e$. Accounting for the (unusual) case when $v_e > v_o$, the TWPD velocity-mismatch photocurrent impulse response is

$$i_{\rm vm}\left(t + \frac{\ell}{v_e}\right) = \frac{Q}{2}\left[|\omega_f| e^{\omega_f t}u(-\omega_f t) + \gamma\omega_r e^{-\omega_r t}u(t)\right] \quad (10)$$

for $\min(\ell/v_o, \ell/v_e) \le t \le \ell/v_o + 2\ell/v_e$ and zero elsewhere, where

$$\omega_f = \Gamma\alpha v_e/(1 - v_e/v_o) \quad (11a)$$

$$\omega_r = \Gamma\alpha v_e/(1 + v_e/v_o) \quad (11b)$$

are characteristic frequencies of the forward and reverse waves. Equation (10) is a general description of the current response of a TWPD to an optical impulse applied at its input considering only velocity mismatch.

Fig. 11 depicts the propagation of a light impulse and the photogenerated electrical waves on a TWPD, showing the formation of the velocity-mismatch impulse response in space. (A temporal velocity-mismatch impulse response from (10) is plotted in [7].) The response is composed of two exponential components, which in general have different decay constants. Conservation of energy and charge requires that the integral of the photocurrent response of an infinitely long TWPD with $\gamma = 1$ equal the total charge available in the optical pulse $Q = N_{\rm ph}(0)\eta_i q = E_0\eta_i q/h\nu$, where E_0 is the total energy in the optical impulse. Furthermore, conservation of momentum for the electrical waves dictates that the total charge be equally split between the forward- and reverse-traveling photocurrent components. As a result, the heights of these two components are generally different where they meet, forming a discontinuity in the photocurrent response at that point.

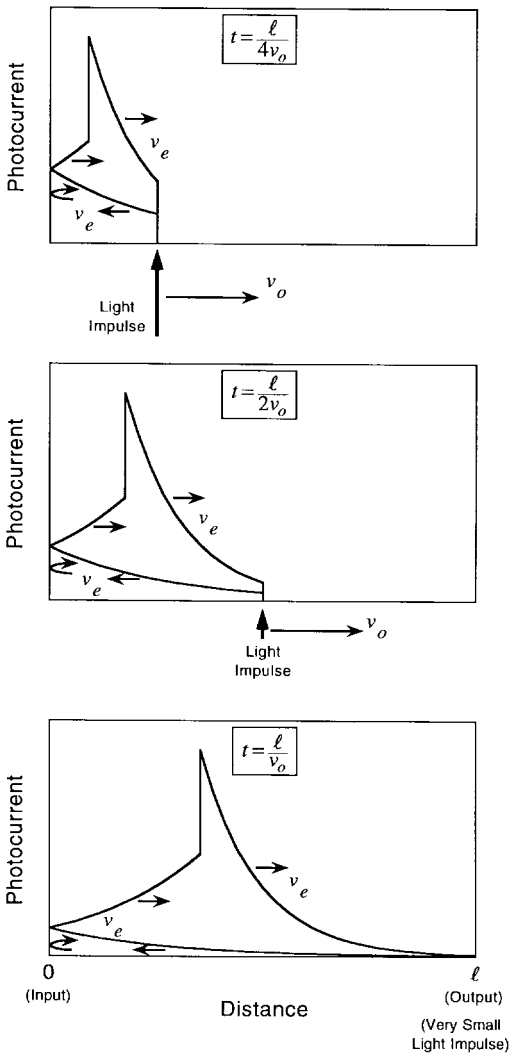

Fig. 11. Spatial plots of the velocity-mismatch impulse response when the light impulse is at $\ell/4$ (top plot), in the middle (center plot), and at the output end (bottom plot) of a TWPD with open-circuit input termination ($\gamma = 1$).

The velocity-mismatch impulse response can be made much shorter by placing a matched termination at the input end of the TWPD ($\gamma = 0$). The reflected wave is then absorbed and only the first term in (10) remains. However, half of the photocurrent is lost in the termination. This is discussed further in the frequency domain in the following section.

D. Velocity-Mismatch Bandwidth Limitation

The velocity-mismatch frequency response is the Fourier transform of the impulse response (10). For long TWPD's, ($\Gamma\alpha\ell \gg 1$), this is given by

$$\frac{i_{\rm vm}(\omega)}{Q} = \frac{1}{2}\left[\frac{\omega_f}{\omega_f - j\omega} + \gamma(\omega)\frac{\omega_r}{\omega_r + j\omega}\right]e^{-j\omega\frac{\ell}{v_e}} \quad (12)$$

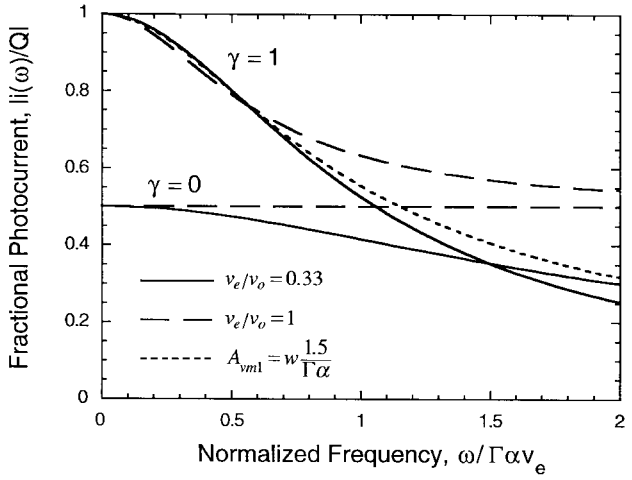

Fig. 12. Velocity-mismatch electrical-frequency responses for velocity matched $(v_e/v_o = 1)$ and mismatched $(v_e/v_o = 0.33)$ TWPD's with open-circuit $(\gamma = 1)$ and matched $(\gamma = 0)$ input terminations. Also shown is the effective area approximation.

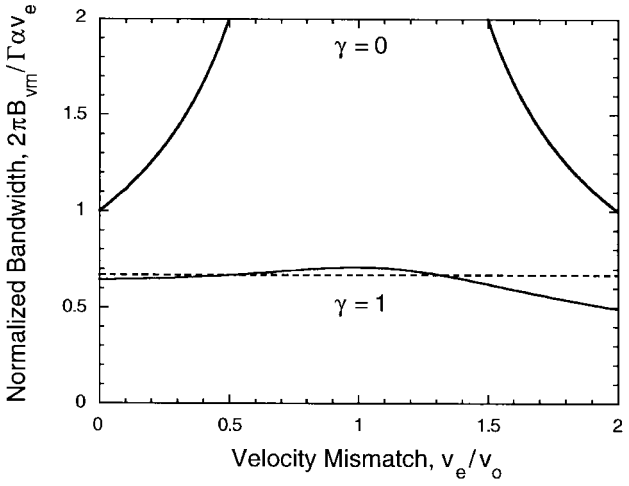

Fig. 13. Normalized 3-dB electrical bandwidths of $\gamma = 1$ and $\gamma = 0$ TWPD's versus velocity mismatch. The broken line shows the constant approximation $(1/1.5)$ to the $\gamma = 1$ curve.

in terms of fractional photocurrent. The photocurrent response for $\gamma = 0$ reduces to a single-pole response with a 3-dB electrical bandwidth limitation of $B_{\rm vm0} = \omega_f/2\pi$, since only the forward-traveling wave contributes.

The TWPD with matched input termination $(\gamma = 0)$ has greater immunity to in-band response ripple resulting from an impedance mismatch at the end of a long transmission line. However, TWPD's, while optically long, generally can be electrically short ($\ll$1 ps), and the electrical distance from a TWPD input to an amplifier input can be much shorter than the shortest wavelength of interest. Undesirable circuit effects resulting when a TWPD with open-circuit input termination $(\gamma = 1)$ is connected to a mismatched load can be designed to occur above the highest frequency of interest.

Fig. 12 shows the effects of velocity-mismatch on the velocity-mismatch frequency responses of TWPD's having open-circuit $(\gamma = 1)$ and matched $(\gamma = 0)$ input terminations. In the velocity-mismatched case $(v_e/v_o = 0.33)$, the $\gamma = 1$ curve intersects the $\gamma = 0$ curve at the -3 dB point of the $\gamma = 0$ response, so the TWPD response with open-circuit input termination $(\gamma = 1)$ is larger than that of the TWPD with matched input termination $(\gamma = 0)$ over its entire bandwidth.

The TWPD with matched input termination $(\gamma = 0)$ has no bandwidth limitation in the velocity-matched case $v_e/v_o = 1$, but is still limited to 50% efficiency. The velocity-matched $\gamma = 1$ curve is always above the $\gamma = 0$ curve. The net bandwidths of TWPD's are limited by other factors, and the overall bandwidth-efficiency product is generally worse in devices with matched $(\gamma = 0)$ input terminations [7].

Comparing the $\gamma = 1$ curves in Fig. 12, it appears that velocity matching has little effect on their 3-dB electrical bandwidths. Fig. 13 confirms that the $\gamma = 1$ curve is almost independent of velocity mismatch, while the $\gamma = 0$ curve is strongly dependent. In the time domain, the response of a $\gamma = 1$ TWPD is composed of forward- and reverse-traveling waves. While velocity matching compresses the temporal duration of the forward-traveling wave, it stretches the reverse-traveling wave, so the overall duration of the $\gamma = 1$ response changes little. As illustrated in Fig. 13, the velocity-mismatch bandwidth limitation for a $\gamma = 1$ TWPD is approximated by

$$B_{\rm vm1} \approx \frac{\Gamma\alpha v_e}{3\pi} \tag{13}$$

independent of optical velocity, with less than 6% error over the entire range of velocities from completely mismatched to beyond matched $0 \le v_e/v_o \le 1.47$. Increasing the electrical velocity increases the velocity-mismatch bandwidth limitation, but velocity-matching is surprisingly of almost no direct value. In fact, the mismatched case, where $v_e/v_o > 1$, is preferable to the matched case $v_e/v_o = 1$, given the same optical velocity.

The velocity-mismatch bandwidth limitation for $\gamma = 1$ in (13) can be cast in a more familiar form by a simple substitution for the electrical velocity from the standard lossless transmission line equations

$$B_{\rm vm1} \approx \frac{1}{2\pi Z_0 C} \cdot \frac{\Gamma\alpha}{1.5}. \tag{14}$$

Evidently, the $\gamma = 1$ TWPD velocity-mismatch bandwidth limitation is comparable to the *RC* bandwidth limitation for a WGPD of fixed area

$$A_{\rm vm1} = w\frac{1.5}{\Gamma\alpha} \tag{15}$$

where w is the waveguide width. In fact, this area can be used to approximate the frequency response up to the velocity-mismatch bandwidth limitation with less than 4% error, as illustrated in Fig. 12. In practice, TWPD overall bandwidth can be found by replacing the device physical junction area in standard lumped-element calculations with the velocity-mismatch effective area.

The effective length in (15), $\ell_{\rm vm1} = 1.5/\Gamma\alpha$, would allow only 78% internal quantum efficiency in a WGPD of the same bandwidth. However, the TWPD can be made much longer physically to achieve close to 100% internal quantum efficiency without sacrificing bandwidth. This is the main advantage of the TWPD.

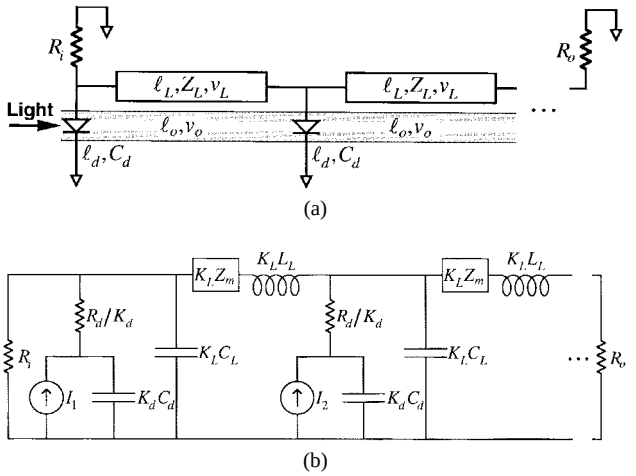

Fig. 14. Periodic TWPD (a) conceptual model showing a transmission line loaded by discrete photodiodes in an optical waveguide and (b) equivalent circuit diagram, including scaling factors which account for lengths of photodetector and transmission-line sections relative to the optical waveguide.

E. Periodic TWPD

The analysis thus far has focused on continuous or fully distributed TWPD's. A periodic TWPD, in which discrete photodetectors in an optical waveguide connect to an electrical transmission line [33], [34], has similar characteristics and can be analyzed using similar methods. Two advantages of a periodic structure are greater design flexibility and reduced electrical loss. However, the periodic TWPD has several practical disadvantages. Fabrication would be much more complicated than for a fully distributed TWPD. Optical reflections and scattering can degrade the bandwidth and efficiency, and microwave loss may still be significant for very long devices.

A conceptual model of a periodic TWPD is depicted in Fig. 14(a). The discrete photodetector elements are placed periodically in an optical waveguide and connected to an electrical transmission line. The corresponding circuit model is shown in Fig. 14(b). The parallel conductance of the doped semiconductor layers of a fully distributed structure and the associated electrical attenuation can be largely eliminated in a periodic structure. The inductance is approximately that of the transmission line, and the capacitance is the sum of the diode and transmission-line contributions. The photodiode, optical waveguide, and transmission-line lengths can be varied independently, so the fractional lengths in Fig. 14(b), $K_L \equiv \ell_L/\ell_o$ and $K_d \equiv \ell_d/\ell_o$, scale the transmission line and photodiode lengths relative to the optical waveguide length.

The flexibility offered by the periodic TWPD would allow techniques such as impedance tapering. A decreasing impedance taper from the TWPD input to the output would continuously reflect the reverse traveling wave, potentially increasing the bandwidth without compromising efficiency. This technique has been used to eliminate the backward wave in traveling-wave amplifiers [35]–[37].

The overall device bandwidth is limited by the bandwidths of the individual photodetector elements and velocity mismatch. The *RC* bandwidth limitations of the discrete photodetectors are calculated from a lumped-element model with load impedance of $Z_{0+}Z_{0-}/(Z_{0+}+Z_{0-})$, where Z_{0+} is the impedance looking forward in the structure and Z_{0-} is the impedance looking backward. The velocity-mismatch impulse response and bandwidth limitation of a constant-impedance structure are given by (10) and (12) with $\Gamma\alpha$ replaced by $\Gamma\alpha \cdot K_d/K_L$.

The parameters for a velocity-matched periodic TWPD are found with appropriate substitutions in the standard lossless transmission-line equations for characteristic impedance and phase velocity

$$\frac{Z_L^2}{Z_0^2} = \frac{(v_L/K_L)^2}{v_o^2} = 1 + \frac{K_d C_d}{K_L C_L} \tag{16}$$

where Z_L and Z_0 are the characteristic impedances of the unloaded and loaded transmission lines, v_L is the phase velocity of the unloaded transmission line, and C_L and C_d are the capacitances per unit length of the unloaded transmission line and the photodiode. The optical group velocity v_o is set equal to the phase velocity of the loaded transmission line. Implicit in these equations are constraints on the characteristic impedance and fractional lengths, $1 \le Z_L/Z_0 \le n_{\text{eff}}$, $1 \le K_L \le n_{\text{eff}}$, and $0 \le K_d \le 1$, where n_{eff} is the effective index of refraction of the linear optical waveguide. The largest fractional photodiode length and shortest electrical length, giving the maximum bandwidth and minimum total microwave loss, occur when the transmission-line lengths are equal to the optical waveguide lengths, $K_L = 1$.

III. Conclusion

The theory of distributed photodetection explains the effects by which TWPD's are capable of larger bandwidth-efficiency products than lumped-element devices, and it provides techniques for design and analysis of TWPD's. A wave model supports equivalent-circuit representations of TWPD's that accurately model complex propagation constant and characteristic impedance. The output characteristic impedance of a TWPD is defined to be matched to that of the load. The mismatch between the velocity of the optical wave and the velocities of the photogenerated electrical waves limits TWPD bandwidth, as does microwave loss.

The velocity-mismatch impulse response is determined by the absorption coefficient and the optical-group and electrical-phase velocities. It is generally characterized by two exponential components due to forward- and reverse-traveling photogenerated electrical waves. The velocity-mismatch impulse response can be arbitrarily short with the quantum efficiency limited to 50% by absorbing the reverse-traveling wave in a matched input termination. However, devices with open-circuit input terminations are generally more efficient over a given bandwidth.

To first order, the velocity-mismatch bandwidth limitation of devices with open-circuit input terminations is actually independent of the mismatch between the electrical and optical velocities, but depends linearly on the electrical velocity and absorption coefficient. This leads to a simple interpretation. The velocity-mismatch bandwidth limitation of a TWPD with open-circuit input termination is comparable to a lumped *RC* bandwidth limitation where the effective area determining the capacitance is 1.5 absorption lengths times the device

width. Thus, the frequency response of a TWPD is essentially independent of its physical length, and nearly 100% internal quantum efficiency can be attained without sacrificing bandwidth. Furthermore, expressing the velocity-mismatch frequency response in terms of an effective *RC* frequency response provides a reasonably accurate means of using traditional design methods.

A discretized periodic TWPD offers additional degrees of freedom in design and potential performance advantages over the fully distributed version at a cost of increased complexity. In this type of device, the electrical propagation characteristics are largely decoupled from the photodiode design, so techniques such as impedance tapering may be used to improve bandwidth without sacrificing efficiency. Design and analysis techniques follow from those for fully distributed TWPD's.

REFERENCES

[1] J. E. Bowers and C. A. Burrus, Jr., "Ultrawide-band long-wavelength p-i-n photodetectors," *J. Lightwave Technol.*, vol. LT-5, pp. 1339–1350, Oct. 1987.

[2] F. K. Reinhart, "Electroabsorption in AlyGa1-yAs-AlxGa1-xAs double heterostructures," *Appl. Phys. Lett.*, vol. 22, no. 8, pp. 372–374, Apr. 1973.

[3] J. L. Merz and R. A. Logan, "Integrated GaAs-AlxGa1-xAs injection lasers and detectors with etched reflectors," *Appl. Phys. Lett.*, vol. 30, no. 10, pp. 530–533, May 1977.

[4] A. Alping and S. T. Eng, "Detection at Gbit/s rates with a TJS GaAlAs laser," *Opt. Commun.*, vol. 44, no. 6, pp. 381–383, Feb. 1983.

[5] J. E. Bowers and C. A. Burrus, "High-speed zero-bias waveguide photodetectors," *Electron. Lett.*, vol. 22, no. 17, pp. 905–906, Aug. 1986.

[6] A. Alping, "Waveguide pin photodetectors: Theoretical analysis and design criteria," *Proc. Inst. Elect. Eng.*, vol. 136, pt. J, no. 3, pp. 177–182, June 1989.

[7] K. S. Giboney, M. J. W. Rodwell, and J. E. Bowers, "Traveling-wave photodetectors," *IEEE Photon. Technol. Lett.*, vol. 4, pp. 1363–1365, Dec. 1992.

[8] H. F. Taylor, O. Eknoyan, C. S. Park, K. N. Choi, and K. Chang, "Traveling wave photodetectors," *Proc. SPIE–Int. Soc. Opt. Eng.*, vol. 1217, pp. 59–63, 1990.

[9] V. M. Heitala and G. A. Vawter, "A large-bandwidth high-quantum-efficiency traveling-wave photodetector based on a slow-wave coplanar transmission line," presented at the *Prog. Electromagnetics Res. Symp.*, Cambridge, MA, July 1991.

[10] V. M. Hietala, G. A. Vawter, T. M. Brennan, and B. E. Hammons, "Traveling-wave photodetectors for high-power, large bandwidth applications," *IEEE Trans. Microwave Theory Tech.*, vol. 43, pp. 2291–2298, Sept. 1995.

[11] K. Giboney, R. Nagarajan, T. Reynolds, S. Allen, R. Mirin, M. Rodwell, and J. Bowers, "172 GHz, 42% quantum efficiency p-i-n travelling-wave photodetector," presented at the *52nd Annu. Device Res. Conf.*, Boulder, CO, June 1994, vol. VIA-9.

[12] K. S. Giboney, "Travelling-wave photodetectors," Ph.D. dissertation, Dept. Elect. and Comput. Eng., Univ. California at Santa Barbara, Aug. 1995.

[13] K. S. Giboney, R. L. Nagarajan, T. E. Reynolds, S. T. Allen, R. P. Mirin, M. J. W. Rodwell, and J. E. Bowers, "Travelling-wave photodetectors with 172 GHz bandwidth and 76 GHz bandwidth-efficiency product," *IEEE Photon. Technol. Lett.*, vol. 7, pp. 412–414, Apr. 1995.

[14] K. Giboney, J. Bowers, and M. Rodwell, "Travelling-wave photodetectors," in *1995 IEEE MTT-S Microwave Symp. Dig.*, Orlando, FL, May 15–19, 1995, pp. 159–162.

[15] H. Guckel, P. A. Brennan, and I. Palócz, "A parallel-plate waveguide approach to microminiaturized, planar transmission lines for integrated circuits," *IEEE Trans. Microwave Theory Tech.*, vol. MTT-15, pp. 468–476, Aug. 1967.

[16] H. Hasegawa, M. Furukawa, and H. Yanai, "Properties of microstrip line on Si–SiO_2 system," *IEEE Trans. Microwave Theory Tech.*, vol. MTT-19, pp. 869–881, Nov. 1971.

[17] D. Jäger, "Slow-wave propagation along variable Schottky-contact microstrip line," *IEEE Trans. Microwave Theory Tech.*, vol. MTT-24, pp. 566–573, Sept. 1976.

[18] Y. Fukuoka and T. Itoh, "Analysis of slow-wave phenomena in coplanar waveguide on a semiconductor substrate," *Electron. Lett.*, vol. 18, no. 14, pp. 598–590, July 1982.

[19] Y. Fukuoka, Y. C. Shih, and T. Itoh, "Analysis of slow-wave coplanar waveguide for monolithic integrated circuits," *IEEE Trans. Microwave Theory Tech.*, vol. MTT-31, pp. 567–573, July 1983.

[20] R. Sorrentino, G. Leuzzi, and A. Silbermann, "Characteristics of metal–insulator–semiconductor coplanar waveguides for monolithic microwave circuits," *IEEE Trans. Microwave Theory Tech.*, vol. MTT-32, pp. 410–416, Apr. 1984.

[21] C. K. Tzuang and T. Itoh, "Finite-element analysis of slow-wave Schottky contact printed lines," *IEEE Trans. Microwave Theory Tech.*, vol. MTT-34, pp. 1483–1489, Dec. 1986.

[22] T. G. Livernois and P. B. Katehi, "A generalized method for deriving the space-domain Green's function in a shielded, multilayer substrate structure with applications to MIS slow-wave transmission lines," *IEEE Trans. Microwave Theory Tech.*, vol. 37, pp. 1761–1767, Nov. 1989.

[23] J. C. Liou and K. M. Lau, "A solution to characteristics of planar transmission lines made of finite-thickness metal on multi-layer media," in *1990 IEEE MTT-S Microwave Symp. Dig.*, May 8–10, 1990, pp. 179–182.

[24] K. Wu and R. Vahldieck, "Hybrid-mode analysis of homogeneously and inhomogeneously doped low-loss slow-wave coplanar transmission lines," *IEEE Trans. Microwave Theory Tech.*, vol. 39, pp. 1348–1360, Aug. 1991.

[25] J. P. K. Gilb and C. A. Balanis, "MIS slow-wave structures over a wide range of parameters," *IEEE Trans. Microwave Theory Tech.*, vol. 40, pp. 2148–2154, Dec. 1992.

[26] J. C. Liou and K. M. Lau, "Analysis of slow-wave transmission lines on multi-layered semiconductor structures including conductor loss," *IEEE Trans. Microwave Theory Tech.*, vol. 41, pp. 824–829, May 1993.

[27] C. Seguinot, P. Kennis, P. Pribetich, and J. F. Legier, "Analytical model of the Schottky contact coplanar line," in *Proc. 14th European Microwave Conf.*, Sept. 1984, pp. 160–165.

[28] Y. R. Kwon, V. M. Hietala, and K. S. Champlin, "Quasi-TEM analysis of slow-wave mode propagation on coplanar microstructure MIS transmission lines," *IEEE Trans. Microwave Theory Tech.*, vol. MTT-35, pp. 545–551, June 1987.

[29] V. M. Hietala, "A study of MIS coplanar slow-wave transmission lines on Silicon," Ph.D. dissertation, Dept Elect. Eng., Univ. Minnesota, Minneapolis, MN, Aug. 1988.

[30] V. M. Hietala and K. S. Champlin, "Measurement of the microwave properties of micron-sized coplanar transmission lines," *J. Electromagnetic Waves and Applicat.*, vol. 5, no. 4/5, pp. 439–452, 1991.

[31] E. Tuncer and D. P. Neikirk, "Highly accurate quasistatic modeling of microstrip lines over lossy substrates," *IEEE Microwave Guided Wave Lett.*, vol. 2, pp. 409–411, Oct. 1992.

[32] The MathWorks, Inc., *The Student Edition of Matlab Version 4*. Englewood Cliffs, NJ: Prentice-Hall, 1995.

[33] M. C. Wu and T. Itoh, "Ultrafast photonic-to-microwave transformer (PMT)," presented at the *LEOS Summer Topical Meeting Opt. Microwave Interactions*, Santa Barbara, CA, July 19–21, 1993.

[34] L. Y. Lin, M. C. Wu, T. Itoh, T. A. Vang, R. E. Muller, D. L. Sivco, and A. Y. Cho, "Velocity-matched distributed photodetectors with high-saturation power and large bandwidth," *IEEE Photon. Technol. Lett.*, vol. 8, pp. 1376–1378, Oct. 1996.

[35] T. T. Y. Wong, *Fundamental of Distributed Amplification*. Norwood, MA: Artech House, 1993, ch. 7.

[36] D. C. Espley, "Generation of very short pulses," *J.I.E.E.*, pt. III-a, pp. 314–315, 1946.

[37] D. C. Espley, E. C. Cherry, and M. M. Levy, "The pulse testing of wide-band networks," *J.I.E.E.*, pt. III-a, pp. 1176–1187, 1946.

Kirk S. Giboney (S'89–M'95) was born on July 19, 1960 in Bakersfield, CA. He received the B.S. degree in physics from the University of California at Davis, in 1984, and the Ph.D. degree in electrical engineering from the University of California at Santa Barbara, in 1995.

From 1985 to 1988, he investigated microwave properties and radiation effects in GaAs devices and integrated circuits at McDonnell Douglas Astronautics Company. From 1990 to 1995, he provided high-speed electro-optic measurements technologies to Hughes Research Laboratories. He is currently engaged in optical communications research and development at Hewlett-Packard Laboratories, Palo Alto, CA.

Mark J. W. Rodwell (M'89) received the M.S. and Ph.D. degrees in electrical engineering from Stanford University, Stanford, CA, in 1982 and 1988, respectively.

From 1982 to 1984, he was a member of the technical staff at AT&T Bell Laboratories. He is currently Professor of electrical engineering at the University of California at Santa Barbara. His current research involves millimeter-wave bipolar transistors, integrated circuits for high-speed fiber-optic transmission, THz Schottky-collector resonant-tunnel-diodes, microwave-power amplifiers, Schottky diode integrated circuits for subpicosecond pulse generation and millimeter-wave instrumentation, and microwave circuit design.

Dr. Rodwell is the recipient of a 1989 National Science Foundation Presidential Young Investigator award.

John E. Bowers (S'78–M'81–SM'85–F'93) received the M.S. and Ph.D. degrees from Stanford University, Stanford, CA, in 1978 and 1981, respectively.

He is a Professor in the Department of Electrical and Computer Engineering at the University of California at Santa Barbara, and is the Director of the Multidisciplinary Optical Switching Technology (MOST) Center. He has worked for AT&T Bell Laboratories and Honeywell, and is currently an Optoelectronics Consultant. He has published over 180 papers and holds 16 patents. His primary research interests involve high-frequency optoelectronic devices and physics.

Dr. Bowers is a member of the Optoelectronics Technology Center, and the NSF Science and Technology Center on Quantized Electronic Structures (QUEST). He is recipient of the Thomas F. Andrews Prize and the NSF Presidential Young Investigator Award.